Cognitive Computation (2023) 15:1190–1210
https://doi.org/10.1007/s12559-021-09954-2

Robust Resting-State Dynamics in a Large-Scale Spiking Neural Network Model of Area CA3 in the Mouse Hippocampus

Jeffrey D. Kopsick[1] · Carolina Tecuatl[2] · Keivan Moradi[1] · Sarojini M. Attili[1] · Hirak J. Kashyap[4] · Jinwei Xing[3] · Kexin Chen[3] · Jeffrey L. Krichmar[3,4] · Giorgio A. Ascoli[1,2]

Received: 5 April 2021 / Accepted: 10 October 2021 / Published online: 28 January 2022

Abstract
Hippocampal area CA3 performs the critical auto-associative function underlying pattern completion in episodic memory. Without external inputs, the electrical activity of this neural circuit reflects the spontaneous spiking interplay among glutamatergic Pyramidal neurons and GABAergic interneurons. However, the network mechanisms underlying these resting-state firing patterns are poorly understood. Leveraging the Hippocampome.org knowledge base, we developed a data-driven, large-scale spiking neural network (SNN) model of mouse CA3 with 8 neuron types, 90,000 neurons, 51 neuron-type specific connections, and 250,000,000 synapses. We instantiated the SNN in the CARLsim4 multi-GPU simulation environment using the Izhikevich and Tsodyks-Markram formalisms for neuronal and synaptic dynamics, respectively. We analyzed the resultant population activity upon transient activation. The SNN settled into stable oscillations with a biologically plausible grand-average firing frequency, which was robust relative to a wide range of transient activation. The diverse firing patterns of individual neuron types were consistent with existing knowledge of cell type-specific activity in vivo. Altered network structures that lacked neuron- or connection-type specificity were neither stable nor robust, highlighting the importance of neuron type circuitry. Additionally, external inputs reflecting dentate mossy fibers shifted the observed rhythms to the gamma band. We freely released the CARLsim4-Hippocampome framework on GitHub to test hippocampal hypotheses. Our SNN may be useful to investigate the circuit mechanisms underlying the computational functions of CA3. Moreover, our approach can be scaled to the whole hippocampal formation, which may contribute to elucidating how the unique neuronal architecture of this system subserves its crucial cognitive roles.

Keywords Neuron-type specific connectivity · Perisomatic-targeting · Dendritic-targeting · Phase · Oscillation · Network dynamics

Introduction

The rodent hippocampal formation has been the subject of extensive investigation since discovery of its critical role in episodic memory consolidation and retrieval [1–3]. Recently formed memories are reinforced and replayed while the rodent is eating, drinking, sleeping, and during quiet wakefulness, a set of behaviors collectively referred to as *resting state* [4, 5]. With an estimated two million neurons [6] and thirty billion synapses [7] in the mouse hippocampal formation, computationally characterizing how resting-state dynamics emerge at the cellular level, and how they relate to other hippocampal functions, is a daunting task. Different scales to explore resting-state functions range from the molecular to the systems level, each conferring distinct descriptions and potential insights.

An intermediate level of description relies on the notion of *neuron types*. While no two cells are ever exactly alike, neurons display distinct patterns of similarities and differences [8]. In practice, neuroscientists routinely classify neurons based on morphological, physiological, and molecular

✉ Giorgio A. Ascoli
ascoli@gmu.edu

[1] Interdepartmental Program in Neuroscience, George Mason University, Fairfax, VA, USA

[2] Bioengineering Department, Volgenau School of Engineering, George Mason University, Fairfax, VA, USA

[3] Department of Cognitive Sciences, University of California, Irvine, Irvine, CA, USA

[4] Department of Computer Science, University of California, Irvine, Irvine, CA, USA

properties [9]. This level of description is the focus of Hippocampome.org, a knowledge base of neuron types in the rodent hippocampal formation [10]. Hippocampome.org identifies neuron types based on their primary neurotransmitter (glutamate or GABA) and the presence of axons and dendrites across distinct anatomical regions and layers [11]. These axonal and dendritic distributions are then leveraged to define the circuit of potential connectivity at the neuron type level [12]. In this framework, a *potential connection type* is associated with a directional pair of one presynaptic and one postsynaptic neuron type [13]. This resource describes 122 neuron types and 3120 potential connection types throughout the hippocampal formation [14], with examples in area CA3 such as Pyramidal, Axo-axonic, and Bistratified. For every neuron type, Hippocampome.org also provides dense coverage of properties such as the expression of specific molecules [15], biophysical membrane properties (e.g., input resistance and resting potential), and electrophysiological firing patterns [16].

The long-term goal of the Hippocampome.org project is to create a computational model of the rodent hippocampal formation as a full-scale spiking neural network (SNN) simulation [17]. Building this SNN needs to account for the population size of each neuron type [18] and their input/output properties [19], along with the probability of connection of each potential connection [20] and their synaptic signal features [21]. A data-driven SNN integrating parameter estimates for each of these characteristics is very challenging to create and requires considerable computational resources to simulate. Nevertheless, we believe this particular description level will have strong explanatory power. Textbook hypotheses about the hippocampal formation (e.g., spatial navigation or pattern separation, completion, and comparison) can be tested based on existing knowledge and will allow for new hypotheses to emerge if the current ones do not hold. Data-driven parameter estimates can be updated when the simulated dynamics do not match the experimental observations. In this manner, simulations become like jigsaw puzzles, where poor-fitting pieces can be swapped for more suitable alternatives, enabling an effective theory–experiment loop.

In this work, we stepped further towards realizing the vision of Hippocampome.org, with a focus on investigating the mechanisms of resting-state dynamics. Specifically, we chose to build a large-scale SNN of the mouse CA3 utilizing eight neuron types (one excitatory principal cell type and seven inhibitory interneuron types) and their 51 potential connections. The diversity of these excitatory and inhibitory elements is important for establishing and maintaining the balanced activity exhibited during resting-state dynamics [22, 23]. This choice is complementary to prior efforts in the dentate gyrus (DG) [24, 25] and CA1 [26, 27]. This network model consists of approximately 90,000 neurons and 250 million synapses. Running a simulation of this size currently exceeds the computational power of standard central processing units (CPUs). We have overcome this issue by instantiating the model in the open-source CARLsim4 simulation environment, which is optimized to run on massively parallel graphical processing units (GPUs) [28]. The simulated CA3 SNN was able to spontaneously generate rhythmic network activity that was stable and robust when provided synchronous or asynchronous transient stimulation over a broad array of intensities. Individual neuron types fired in frequency ranges consistent with those observed during resting-state behaviors in vivo. Simulations involving altered network structures lacking either neuron- or connection-type specificity were neither stable nor robust, highlighting the importance of circuit architecture in building stable and robust large-scale SNNs. Moreover, the incorporation of external input from DG Granule cells to the CA3 SNN generated slow gamma oscillations, demonstrating that the model can produce oscillations observed in CA3 and that the framework is flexible to the addition of new features to test hypotheses on the hippocampal formation.

Methods

Neuron and Connection Types

Hippocampome.org defines neuron types based on their primary neurotransmitter (glutamate or GABA) and the presence of axons and dendrites across distinct layers: in the case of area CA3, strata lacunosum-moleculare (SLM), radiatum (SR), lucidum (SL), pyramidale (SP), and oriens (SO). For example, Hippocampome.org defines a CA3 Pyramidal cell as a glutamatergic neuron with dendrites in all 5 layers (SO, SP, SL, SR, and SLM) and axons in SO and SR; whereas a CA3 QuadD-LM cell is a GABAergic neuron with dendrites in SO, SP, SL, and SR and axons in SLM. The presence of the axons of a presynaptic neuron type and dendrites of a postsynaptic neuron type within the same layer of CA3 identifies a connection type. For example, since CA3 Pyramidal cells and CA3 QuadD-LM cells have axons and dendrites in SR, respectively, they constitute a connection type (from the Pyramidal neuron type to the QuadD-LM neuron type).

Neuron Type Selection

The full-scale CA3 network consisted of Pyramidal cells and seven interneuron types: Axo-axonic, Basket, Basket CCK+, Bistratified, Ivy, Mossy Fiber-Associated ORDEN (MFA ORDEN), and QuadD-LM cells (Fig. 1). The choice of neuron types was based on the following

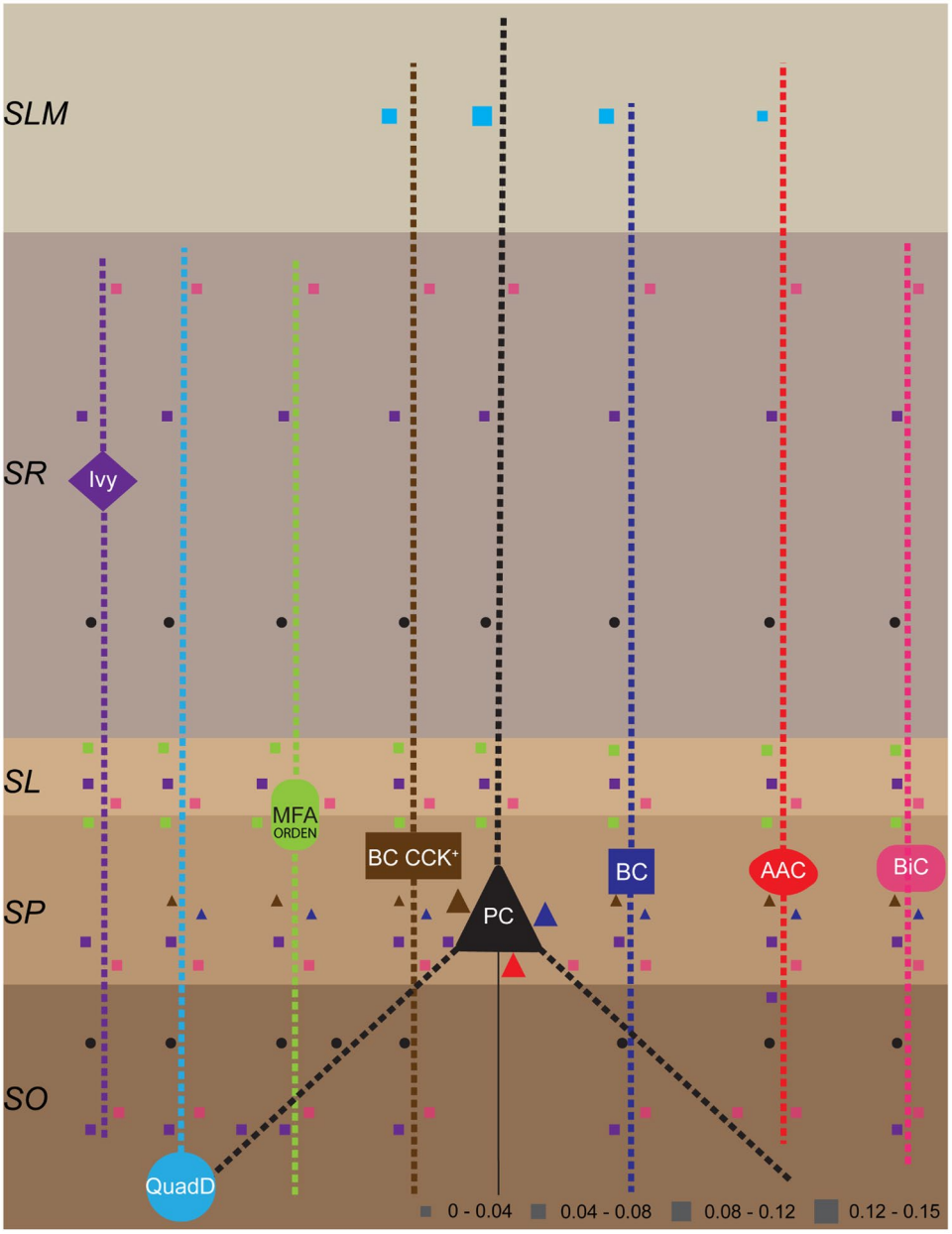

Fig. 1 Connectivity of the model CA3 circuit. Connection probabilities from excitatory cells are indicated with a circle, from inhibitory perisomatic cells with a triangle, and from inhibitory dendritic-targeting cells with a square. Relative shape size indicates connection probability (scale at bottom right). Dotted lines indicate the laminar extent of the dendritic tree for each neuron type to explain the connectivity, but neurons are simulated as single compartments in our network. QuadD, QuadD-LM; PC, Pyramidal cell; BC, Basket cell; AAC, Axo-axonic cell; BiC, Bistratified cell; SLM, stratum lacunosum-moleculare; SR, stratum radiatum; SL, stratum lucidum; SP, stratum pyramidale; SO, stratum oriens

rationale: (1) one excitatory cell type, which served as the main readout for the network, and (2) selection of at least one interneuron type for each major inhibitory pathway in this area, namely, perisomatic-targeting with axons in SP (Axo-axonic, Basket, Basket CCK+), collateral-related with axons in SO and SR (Bistratified and Ivy), mossy fiber associated with axons in SL (MFA ORDEN), and perforant pathway-associated with axons in SLM (QuadD-LM, a type of O-LM cell). For firing frequency analysis and for alternate networks, non-perisomatic interneuron types were grouped as dendritic-targeting (Bistratified, Ivy, MFA ORDEN, QuadD-LM). Based on axonal-dendritic overlaps as described above, these 8 neuron types give rise to 51 connection types.

Biologically Realistic Parameter Selection

Hippocampome.org annotates neuron and connection types with quantitative properties (i.e., parameters) necessary to simulate them. Model parameters can be divided into two broad categories: those describing neurons and those describing synaptic connections. The *neuron category* included a set of parameters that defines the neuronal input–output function, i.e., the spiking pattern produced by a neuron in response to a given stimulation [16]. Hippocampome.org adopted a dynamical systems framework [29] that in its simplest form represents neurons as single compartments using nine parameters [30]: the membrane capacitance (C), a constant that reflects conductance during spike generation

Table 1 Population sizes for neuron types utilized in the network models

	Neuron type	Supertype	Population size
Local circuit	CA3 Pyramidal	Glutamatergic PC:Pyramidal:CA3	74,366
	CA3 Axo-axonic	Perisomatic-targeting:Axo-axonic:CA3	1,909
	CA3 Basket	Perisomatic-targeting:Basket:CA3	515
	CA3 Basket CCK+	Perisomatic-targeting:Basket CCK+:CA3	665
	CA3 Bistratified	Collateral-related:RO-targeting:CA3	4,631
	CA3 Ivy	Ivy/Neurogliaform Family:Ivy/Neurogliaform:CA3	2,334
	CA3 MFA ORDEN	Mossy Fiber-related:L-targeting:CA3	1,526
	CA3 QuadD-LM	O-LM Family:O-LM-Like:CA3	3,280
	Local circuit total		89,226
Local circuit + external afferents	DG Granule	Glutamatergic GC:Granule:DG	394,502
	Total		483,728

CCK + Cholecystokinin positive, *O-LM* oriens-lacunosum moleculare

(k), the resting membrane potential (v_r), the instantaneous threshold potential (v_t), a recovery time constant (a), a constant that reflects conductance during repolarization (b), the spike cutoff value (v_{peak}), the membrane potential reset value (V_{min}), and a constant that reflects the currents activated during a spike (d). Hippocampome.org provides experimentally constrained values of each of these 9 parameters for most neuron types (hippocampome.org/php/Izhikevich_model.php). These parameter values were selected as those best-fitting the firing patterns reported in the literature for the corresponding neuron types [30].

The other parameter in the neuron category was the *population size* that determines the number of neurons of a given type. Numerical optimization was utilized to estimate these population sizes based on relevant published information, such as the laminar location of the soma of the neuron type, its known expression of a given molecule, and the measured density of cells expressing that molecule in that layer [31, 32]. Each neuron type in our network was selected as a representative of a *supertype* as defined in Hippocampome.org. Thus, the population size of each neuron type in our network is the sum of all neuron types of the given supertype. For example, the number of CA3 Axo-axonic cells (i.e., the population size parameter value for this particular neuron type) consisted of the sum of Axo-axonic proper and Horizontal Axo-axonic cells (two variants of Axo-axonic neurons in CA3), which in the model was 1,909. The population sizes and the 9 Izhikevich parameters for each of the 8 CA3 neuron types included in the network summed up to a total of 80 parameter values in the neuron category (Tables 1 and 2).

The *category of parameters describing synaptic connections* included two sets of parameters: one pertaining to synaptic dynamics, i.e., a description of the postsynaptic signal caused by a presynaptic spike and related short-term plasticity (STP), and the other pertaining to connection probability and delay between the presynaptic and the postsynaptic neuron types. To obtain estimates for the synaptic dynamics, synaptic electrophysiology data from over a thousand studies were mined, which included values for variables such as the type of synaptic response (glutamatergic or GABAergic), the reversal potential, the recording method (e.g., whole-cell patch-clamp), the ionic compositions of the intracellular and extracellular solutions, and the receptor-mediated currents that were measured (AMPA or $GABA_A$) [21]. These raw synaptic data were then digitized and integrated using computational modeling and deep learning techniques to obtain normalized parameter estimates for each connection type in our network using the Tsodyks, Pawelzik, and Markram (TPM) STP model [33–35]. Specifically, synaptic dynamics in the TPM model are described by five parameters: the

Table 2 Izhikevich parameters by neuron type

Neuron type	k	a	b	d	C	Vr	Vt	Vmin	Vpeak
CA3 Pyramidal	0.792	0.008	−42.552	588	366	−63.204	−33.604	−38.868	35.861
CA3 Axo-axonic	3.961	0.005	8.684	15	165	−57.100	−51.719	−73.969	27.799
CA3 Basket	0.995	0.004	9.264	−6	45	−57.506	−23.379	−47.556	18.455
CA3 Basket CCK+	0.583	0.006	−1.245	54	135	−58.997	−39.398	−42.771	18.275
CA3 Bistratified	3.935	0.002	16.580	19	107	−64.673	−58.744	−59.703	−9.929
CA3 Ivy	1.916	0.009	1.908	45	364	−70.435	−40.859	−53.400	−6.920
CA3 MFA ORDEN	1.380	0.008	12.933	0	209	−57.076	−39.102	−40.681	16.313
CA3 QuadD-LM	1.776	0.006	−3.449	52	186	−73.482	−54.937	−64.404	7.066

synaptic conductance (g), synaptic decay time constant (τ_d), synaptic resource recovery time constant (τ_r), resource utilization reduction time constant (τ_f), and portion of available resources being utilized on each synaptic event (U). Note that this modeling formalism captures connection-specific *unitary* synaptic communication. As such, it reflects the total somatic effect of all synapses corresponding to connected neuron pairs.

Hippocampome.org provides connection probabilities for all directional pairs of neuron types calculated from the overlap between the axons of a presynaptic neuron type and the dendrites of a postsynaptic neuron type within all individual layers of CA3 (Fig. 1; [20]; hippocampome.org/php/synapse_probabilities_dal.php); these probabilities were scaled for the mouse according to an anatomical scaling factor [36]. The connection probabilities for the 51 potential connections are reported in Table 3. Additionally, our simulation specifies the number of synapses per connection type, which was computed based on the population sizes of the presynaptic and postsynaptic neuron type involved and the directional connection probability between them. For example, the number of synapses from CA3 Pyramidal cells onto CA3 Basket cells was 74,366*515*0.02 = 765,970. While the numbers of synapses are not reported individually for each connection here, they can be computed from the data in Tables 1 and 3 as highlighted in the above example. For synaptic delays, all potential connections with a presynaptic interneuron type were assumed to have delays of 1 ms due to the short length of the local axon. For synapses from the Pyramidal cell as the presynaptic neuron type, delays were assigned based on the assumed axonal conduction velocity of 300 µm/ms [37] and the mean distance that the Pyramidal cell axon traveled within a parcel of CA3 (as also reported in [20]). For example, CA3 Pyramidal cell axons have a somatic length of 633 µm in SR, so we allowed for synaptic delays of either 1 or 2 ms for any postsynaptic type that the Pyramidal cell connected to in SR. The 5 TPM parameters and the synaptic delays for each potential connection are reported in Table 4. Altogether, Tables 2 and 3 account for 357 parameter values describing synaptic connections. Summed with 80 parameter values in the neuron category, the total number of model parameters was 437. All parameter estimates provided (except for population sizes) were computed from in vitro studies. This was sufficient for obtaining realistic responses in the network without the need to conduct a parameter search or employ an optimization technique.

Model Implementation and Execution

The CA3 model was implemented in CARLsim4 [28], which utilized the 4th order Runge–Kutta numerical integration method with a fixed time step of 0.2 ms. Simulation duration was 9 s, with the last 5 s used for analysis. Instantiation and execution of the network model was performed on a single 32 GB VRAM Tesla V100 GPU on the George Mason University High Performance Computing Cluster (ARGO). ARGO, which contained more than twenty such GPUs, allowed for efficient and flexible simulation that greatly reduced the time needed to test different stimulation paradigms and alternate network structures. Simulation results were loaded and visualized in MATLAB with CARLsim4's Offline Analysis Toolbox (OAT). Additional custom-built functions for data analysis were written in MATLAB. All scripts developed are available on GitHub (github.com/Hippocampome-Org/snn_analysis).

Network Stimulation Protocol and Analysis

Two protocols were utilized to initiate network activity: a synchronous stimulation, where a random subset of

Table 3 Connection probability for each connection type in the network model

Pre-post	CA3 Pyramidal	CA3 Axo-axonic	CA3 Basket	CA3 Basket CCK+	CA3 Bistratified	CA3 Ivy	CA3 MFA ORDEN	CA3 QuadD-LM
CA3 Pyramidal	0.025	0.015	0.020	0.017	0.016	0.025	0.021	0.013
CA3 Axo-axonic	0.150							
CA3 Basket	0.150	0.025	0.005	0.005	0.025		0.005	0.005
CA3 Basket CCK+	0.150	0.025	0.005	0.005	0.025		0.005	0.025
CA3 Bistratified	0.028	0.007	0.009	0.004	0.033	0.004	0.009	0.008
CA3 Ivy	0.072	0.004	0.016	0.011	0.017	0.004	0.017	0.002
CA3 MFA ORDEN	0.042	0.004	0.007	0.005	0.005	0.003	0.002	0.004
CA3 QuadD-LM	0.119	0.005	0.067	0.050				
DG Granule	0.002	0.001	0.001	0.001	0.001	0.001	0.001	0.001

Presynaptic cell types are listed in the first column, while postsynaptic cell types are listed in the first row

Table 4 STP parameters and synaptic delays for each connection type in the model

Presynaptic	Postsynaptic	g	τ_d	τ_r	τ_f	U	Synaptic delay
CA3 Pyramidal	CA3 Pyramidal	0.30	10.22	318.51	21.45	0.28	1–2
CA3 Pyramidal	CA3 Axo-axonic	0.65	4.92	630.73	26.26	0.26	1–2
CA3 Pyramidal	CA3 Basket	1.70	3.97	691.42	21.16	0.12	1–2
CA3 Pyramidal	CA3 Basket CCK+	0.85	4.29	530.40	22.45	0.20	1–2
CA3 Pyramidal	CA3 Bistratified	0.62	5.37	569.15	23.85	0.26	1–2
CA3 Pyramidal	CA3 Ivy	1.77	5.67	552.27	26.73	0.12	1–2
CA3 Pyramidal	CA3 MFA ORDEN	1.10	5.95	444.99	29.01	0.15	1–2
CA3 Pyramidal	CA3 QuadD-LM	1.09	5.82	453.29	27.16	0.15	1–2
CA3 Axo-axonic	CA3 Pyramidal	2.71	7.62	361.03	12.93	0.13	1
CA3 Basket	CA3 Pyramidal	2.28	7.64	384.34	16.74	0.13	1
CA3 Basket	CA3 Axo-axonic	2.63	3.80	725.03	23.21	0.19	1
CA3 Basket	CA3 Basket	1.80	3.01	689.51	11.19	0.39	1
CA3 Basket	CA3 Basket CCK+	1.69	4.21	636.76	16.72	0.24	1
CA3 Basket	CA3 Bistratified	2.30	4.72	680.33	16.72	0.18	1
CA3 Basket	CA3 MFA ORDEN	1.36	5.23	581.94	19.60	0.30	1
CA3 Basket	CA3 QuadD-LM	1.31	5.16	589.20	19.31	0.31	1
CA3 Basket CCK+	CA3 Pyramidal	1.89	9.10	376.87	13.76	0.08	1
CA3 Basket CCK+	CA3 Axo-axonic	1.94	5.44	477.43	18.50	0.12	1
CA3 Basket CCK+	CA3 Basket	0.96	4.69	505.12	14.86	0.28	1
CA3 Basket CCK+	CA3 Basket CCK+	0.97	4.89	283.28	23.38	0.12	1
CA3 Basket CCK+	CA3 Bistratified	1.78	5.97	478.31	15.25	0.13	1
CA3 Basket CCK+	CA3 MFA ORDEN	1.02	6.54	421.42	17.84	0.21	1
CA3 Basket CCK+	CA3 QuadD-LM	1.00	6.48	398.15	17.34	0.22	1
CA3 Bistratified	CA3 Pyramidal	2.08	7.49	481.85	16.61	0.12	1
CA3 Bistratified	CA3 Axo-axonic	2.15	4.57	686.28	19.16	0.17	1
CA3 Bistratified	CA3 Basket	1.10	3.86	695.21	14.60	0.37	1
CA3 Bistratified	CA3 Basket CCK+	1.44	4.58	592.19	17.69	0.22	1
CA3 Bistratified	CA3 Bistratified	2.01	4.58	775.04	13.60	0.17	1
CA3 Bistratified	CA3 Ivy	1.34	5.33	649.83	18.17	0.30	1
CA3 Bistratified	CA3 MFA ORDEN	1.57	5.54	605.25	18.30	0.29	1
CA3 Bistratified	CA3 QuadD-LM	1.12	5.53	594.33	17.89	0.30	1
CA3 Ivy	CA3 Pyramidal	2.23	9.01	439.50	23.01	0.12	1
CA3 Ivy	CA3 Axo-axonic	2.29	5.67	651.64	25.51	0.17	1
CA3 Ivy	CA3 Basket	1.16	4.75	665.16	19.12	0.37	1
CA3 Ivy	CA3 Basket CCK+	1.54	5.40	614.01	20.98	0.23	1
CA3 Ivy	CA3 Bistratified	2.16	6.24	660.48	22.69	0.17	1
CA3 Ivy	CA3 Ivy	1.34	5.51	675.54	17.72	0.31	1
CA3 Ivy	CA3 MFA ORDEN	1.27	6.96	578.90	28.45	0.30	1
CA3 Ivy	CA3 QuadD-LM	1.18	6.89	563.47	26.15	0.30	1
CA3 MFA ORDEN	CA3 Pyramidal	1.97	7.15	496.05	20.62	0.12	1
CA3 MFA ORDEN	CA3 Axo-axonic	2.12	4.55	762.60	21.45	0.16	1
CA3 MFA ORDEN	CA3 Basket	1.08	3.90	759.12	15.70	0.36	1
CA3 MFA ORDEN	CA3 Basket CCK+	1.42	4.32	693.92	17.08	0.22	1
CA3 MFA ORDEN	CA3 Bistratified	2.00	4.96	776.57	17.27	0.17	1
CA3 MFA ORDEN	CA3 Ivy	1.35	5.39	712.27	21.22	0.30	1
CA3 MFA ORDEN	CA3 MFA ORDEN	1.16	5.53	642.10	22.52	0.29	1
CA3 MFA ORDEN	CA3 QuadD-LM	1.10	5.52	637.95	21.01	0.29	1
CA3 QuadD-LM	CA3 Pyramidal	1.72	9.11	382.14	24.79	0.11	1
CA3 QuadD-LM	CA3 Axo-axonic	1.91	5.17	635.01	22.34	0.15	1
CA3 QuadD-LM	CA3 Basket	1.00	4.29	663.25	16.42	0.34	1

Table 4 (continued)

Presynaptic	Postsynaptic	g	τ_d	τ_r	τ_f	U	Synaptic delay
CA3 QuadD-LM	CA3 Basket CCK+	1.31	4.83	596.50	17.78	0.21	1
DG Granule	CA3 Pyramidal	1.83	7.43	347.44	42.00	0.16	1–10
DG Granule	CA3 Axo-axonic	1.94	4.13	702.40	36.83	0.17	1–10
DG Granule	CA3 Basket	1.50	3.58	744.66	30.29	0.19	1–10
DG Granule	CA3 Basket CCK+	1.57	3.46	658.70	25.92	0.21	1–10
DG Granule	CA3 Bistratified	1.91	4.39	594.72	38.34	0.19	1–10
DG Granule	CA3 Ivy	2.27	3.75	764.65	21.48	0.18	1–10
DG Granule	CA3 MFA ORDEN	1.97	4.87	453.65	48.65	0.19	1–10
DG Granule	CA3 QuadD-LM	1.88	4.96	464.59	43.06	0.18	1–10

Pyramidal cells was selected and fired transiently in the first millisecond of the simulation, and an asynchronous stimulation, where a random Pyramidal cell subset was chosen to fire at different times during the first second of the simulation. We stimulated each Pyramidal cell only once in either protocol. The size of the random subsets for synchronous stimulation ranged from 100 to 1,000 Pyramidal cells, and the random subsets for asynchronous stimulation in each millisecond ranged from 1 to 25 Pyramidal cells (for a total of up to 1,000 to 25,000 Pyramidal cells activated). Once the input terminated, the simulation ran for an additional 9 s after synchronous stimulation or 8 s after asynchronous stimulation to evaluate network dynamics beyond the transient initiation. Activity from the eight neuron types was measured via CARLsim4, which captured spike information in Address Event Representation (AER) format (i.e., unique spike times for each neuron in each group) in 1 ms intervals. Spike times were stored in .dat files (a generic data file extension) for each neuron type, which enabled simple retrieval of the binned spike counts for every neuron.

Of note, we updated CARLsim4 in two important aspects for this work. First, we enabled the specification of short-term synaptic plasticity parameter values at the level of connection type, whereas before CARLsim4 defined these parameters solely based on the identity of the presynaptic neuron. Second, we implemented a NeuronMonitor function to capture the instantaneous membrane potential (recorded in mV) and input current (recorded in pA) of each neuron. These data also were stored at 1 ms intervals in .dat files.

Spike, voltage, and current data associated with each neuron type were loaded into MATLAB at 1 ms intervals using CARLsim4's SpikeReader and NeuronReader tools. A first approximation local field potential (LFP) was computed from the average voltage of every neuron in a desired group. The LFP was calculated separately for each neuron type, collectively for all perisomatic neuron types and for all dendritic-targeting neuron types, as well as for the entire network. The power spectral densities (PSD) of the LFPs were derived as the absolute square of the fast Fourier transform amplitude. Sharp-wave ripple (SWR) events were detected using the LFP band-pass filtered in the 150–200 Hz range when the power exceeded two standard deviations (SD) of the mean power during the course of the simulation and lasted at least 15 ms [38, 39].

The mean and coefficient of variation (CV) of the inter-spike intervals (ISI) along with the mean firing frequency for each neuron of every neuron type were computed. The mean and SD of the activity sparseness were computed for each neuron type, which was quantified as the percentage of active neurons of each neuron type in 100 ms intervals or over the entire simulation period [40]. Relationships between the mean and CV of ISIs were assessed via Pearson correlation coefficients for the Pyramidal, perisomatic-, and dendritic-targeting groups. Additionally, the inequality in the firing rates of neurons of each type was assessed with a Lorenz curve, which highlighted the cumulative spike share of individual neurons within a type. The Gini coefficient computed from the Lorenz curve quantified the magnitude of the deviation of cumulative spike share from equality. Values of the Gini coefficient can range from zero to one, where zero reflects all neurons having the same number of spikes, and one reflecting that one neuron fired all the spikes.

Preferred firing phases for each neuron type were computed relative to the filtered LFP analog in the observed frequency bands, using all spikes for the given neuron type that occurred within the 5s analysis window. For each filtered LFP analog, the spike times were converted to phases relative to the troughs of the cycle in which they fired. Additionally, the angular SD and mean resultant vector length for each filtered LFP analog were computed for each neuron type with the CircStat MATLAB toolbox [41]. Spike phases were then subjected to a Rayleigh nonuniformity test to determine the level of modulation of the firing for each neuron type [42].

Network stability was evaluated based on two criteria: the CV of the instantaneous firing frequency of the network, computed from the mean and SD of the firing frequency of all neurons (irrespective of their neuron type, binned at 1 ms

intervals), and the mean firing frequencies of each neuron type. The network was considered stable if CV ≤ 1 and each neuron type had a mean firing frequency greater than zero. The robustness of the network was evaluated on the SD of the network's firing frequency within each stimulation paradigm, with a SD less than or equal to 0.25 Hz considered robust.

Alternate Networks

To assess the influence of connection-specific probabilities and the diversity of neuron types, we simplified the network architecture in two ways. The *class* network, which assessed the influence of connection-specific probabilities, preserved all features of the *baseline* network, with the exception that the probabilities of connection for each presynaptic neuron type to their corresponding potential postsynaptic neuron type targets were equal for each connection class (E-E, E-I, I-E, I-I, where "E" and "I" stand for excitatory and inhibitory neuron types, respectively). Additionally, the equivalent connection probabilities ensured that the overall number of synapses created by each connection class in the baseline network was preserved. The *archetype* network, which assessed the influence of the diversity of neuron types, preserved all features of the baseline network, with the exception that only a representative neuron type from the excitatory (Pyramidal), perisomatic (Basket), and dendritic-targeting (MFA ORDEN) types were utilized. The representatives were chosen to ensure that all nine potential connection types (E-E, E-I_P, E-I_D, I_P-E, I_D-E, I_P-I_P, I_P-I_D, I_D-I_P, I_D-I_D, where "D" and "P" stand for dendritic- and perisomatic-targeting neuron types, respectively) were preserved. Each representative reflected the sum of both the population sizes and synapses created by the perisomatic- and dendritic-targeting types in the baseline network, with the Izhikevich and STP parameters preserved for the representative type.

In addition to simplifying the network architecture into the two variants described above, we also *expanded* the baseline architecture to include external inputs from DG. This *DG-CA3* network assessed the influence of mossy fibers on the activity and included an additional neuron type, DG Granule, and eight connection types, with population size, connection probabilities, TPM parameter estimates, and conduction delays as defined in Tables 1, 3, and 4. Each DG Granule cell's mean firing rate was set to 1.5 Hz and was governed by a Poisson process [43].

List of Explicit Reasoned Model Assumptions

A limited number of reasonable assumptions, listed below, were necessary to match the parameters required by the described model design with available experimental measurements.

- The connection probability for a pair of presynaptic and postsynaptic neuron types could be set from a range of estimates between the corresponding supertypes. We assumed that connection types involving the same supertype have similar structural properties and therefore similar connection probabilities.
- The connection probabilities from perisomatic interneurons to Pyramidal cells were set to 0.15. This assumption was based on the observation that perisomatic interneurons contact Pyramidal cells with higher probabilities than dendritic-targeting interneurons [26], which in our model had an upper bound of 0.12.
- The connection probabilities involving a presynaptic perisomatic neuron type were set between 0.005 and 0.025. This assumption was based on the range of connection probabilities for I_D-I_P and I_D-I_D in the network model.
- The connection probability between DG Granule and CA3 Pyramidal was set to 0.002, and connection probabilities between DG Granule and CA3 interneurons were set to 0.001. These probabilities were assumed based on the number of boutons and filopodial extensions provided to CA3 Pyramidal cells and interneurons [44].
- The synaptic delays between DG Granule and CA3 neuron types were set between 1 and 10 ms. These delays assumed that DG Granule cells could span the length of CA3 SL.
- The number of transiently stimulated Pyramidal cells in the baseline network corresponded to the fraction of active Pyramidal cells observed during SWR in vivo, which range from < 1 to > 30% in a single SWR event in CA1 [45]. We assumed that the same proportions held in CA3.

Building Blocks of Full-Scale Network Models

David Marr posited that a complex system such as the brain can be understood at the computational (i.e., what problems does the system solve), algorithmic (i.e., how does the system solve problems), and implementation levels (i.e., the substrate or mechanism within the system that solves the problems) [46, 47]. In the spirit of Marr's three levels of analysis, we have defined a set of conceptual elements that are important to building full-scale network simulations designed to model functions such as memory formation and recall (Table 8). Furthermore, we have provided explanations of the advantage each element could provide when explicitly modeled. Our simulations only employed elements whose parameters could be directly constrained by experimental measurements. This approach allows for empirically testing which building blocks are needed to adequately model a function or behavior.

Results

Here we briefly describe our data-driven CA3 model (the *baseline* network, Fig. 1); a more thorough description can be found in the "Methods" section. We simulated the baseline SNN containing 74,366 (83%) excitatory and 14,860 (17%) inhibitory neurons. These percentages were close to those observed experimentally via immunocytochemical and stereological estimation [48]. The ~250 million synapses in the network were comprised of E-E (~55%), E-I (~8%), I-E (~36%), and I-I (~1%) connections. Each neuron type in the network was instantiated with corresponding population sizes (Table 1) and Izhikevich model parameters (Table 2), and each potential connection type was created with its corresponding connection probability (Table 3, Figs. 1 and 2) and STP parameters (Table 4).

Our updated Hippocampome-CARLsim4 framework enabled the declaration of these neuron and connection-type specific properties critical for testing the stability and robustness of our network. The CARLsim4 Hippocampome CA3 model is publicly available on GitHub (github.com/UCI-CARL/CARLsim4/tree/feat/meansdSTPPost_hc/projects). In the software repository, we provide a detailed guide that describes how to generate data-driven networks and how they could be used to test additional hypotheses of hippocampal function.

We initiated activity in the network via synchronous, transient stimulation of a randomly chosen subset of Pyramidal cells at the beginning of the simulation, or through asynchronous random stimulation of Pyramidal cells within the first second of the simulation. Each chosen Pyramidal cell was stimulated once, and this initial activity in turn activated other Pyramidal cells and interneurons. After a variable delay of current integration, rhythmic activity reliably emerged in the baseline network with both the synchronous and asynchronous protocols, as evidenced in the baseline network's LFP (Fig. 3a). The network displayed a remarkably stable and robust grand average firing frequency (GAF) of ~3 Hz, with low variability within the duration of the recordings, across multiple simulation runs with different subsets of stimulated Pyramidal cells, and over a broad range of transient stimulation paradigms, from 100 cells synchronously to 25,000 cells asynchronously (Fig. 3b). The firing frequencies of individual neuron types varied between 2 and 15 Hz and were compared with values observed during resting-state behaviors in vivo (Table 5). Overall, the average activity of various neuron types was well aligned with their expected characteristics: the non-CCK+ perisomatic

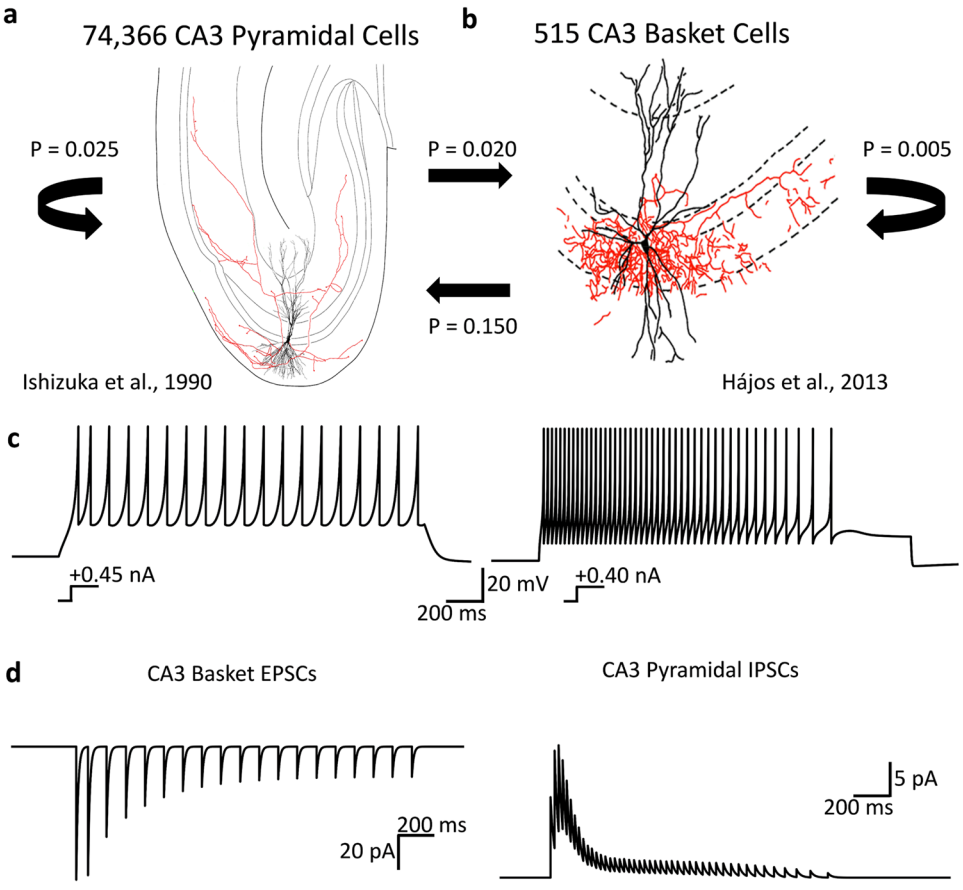

Fig. 2 Required characterization for a representative connection type (CA3 Pyramidal–CA3 Basket) out of the 51 in the CA3 circuit model. **a** Population size of each neuron type [31]. **b** Probability of connection (P) between each directional pair of neuron types [20]. **c** Intrinsic electrophysiological properties of each neuron type [30]. **d** Excitatory (EPSC) and inhibitory post-synaptic currents (IPSC) generated from the spike trains in **b** [21]

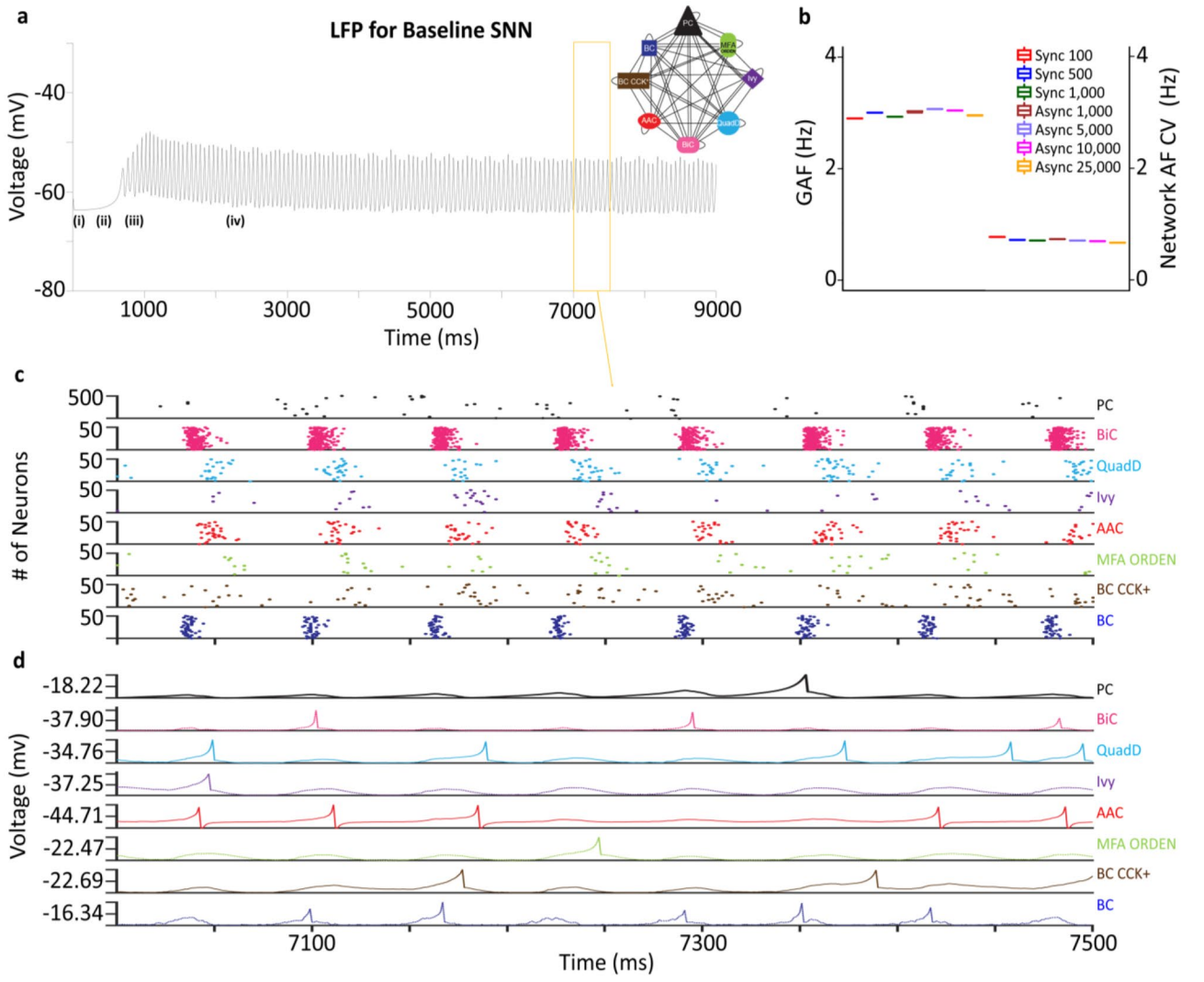

Fig. 3 Population activity for CA3 spiking neural network. **a** First approximation LFP activity. Synchronous stimulation leads to transient network depolarization (i), followed by integration of currents propagating throughout the network for the next 500 ms (ii). With a large number of Pyramidal cells above firing threshold, the network experiences a population burst (iii), before settling into a steady rhythm that will persist for the duration of the recording (iv). Inset: Connectivity schematic for the baseline network. **b** Summary plots for both synchronous and asynchronous stimulation detail low firing rate variability (< 0.2 Hz) and low network CV (< 1), indicative of a stable and robust network. **c** Raster plot of 500 ms activity from (**a**) (yellow frame) of 500 Pyramidal cells and 50 interneurons of each type. **d** Representative voltage trace for each neuron type during 500 ms activity from (**a**)

cells (Basket and Axo-axonic cells) fired at the highest frequency; Pyramidal cells displayed sparse activity (Table 5); and the remaining interneurons (dendritic-targeting or CCK-expressing) varied substantially from low to moderate activity. Additionally, raster plots from a random sample of 500 Pyramidal cells and 50 interneurons of each type (Fig. 3c), along with their example membrane potential traces (Fig. 3d), highlighted their unique firing profiles.

We thus sought to characterize the variability within and across each neuron type. First, we looked at the distributions of the mean firing frequencies of individual neurons that were active within the analysis window (Fig. 4a). The Pyramidal cells and a majority of interneuron types had skewed firing frequency distributions, as previously seen in CA3 Pyramidal cells and interneurons recorded in vivo [45]. We then assessed the contributions that each neuron provides to the firing profile of its corresponding type through their Gini coefficient, which quantifies the deviation from equality with a value between 0 (all neurons contribute an equal number of spikes) and 1 (one neuron contributes all spikes). Gini coefficients ranged between 0.04 and 0.25, indicating moderate firing frequency inequality for Ivy and MFA ORDEN cells and low inequality for all other neuron types (Fig. 4b). Next, we investigated whether the mean interspike interval

Table 5 Firing rates and activity sparseness (portion of active cells in 100 ms) during resting-state behaviors as recorded in our model and those recorded in vivo for the neuron types included in our network model. Firing rates are expressed as mean ± s.d

Neuron type	Synchronous model firing rate (Hz) and activity sparseness (%)	Asynchronous model firing rate (Hz) and activity sparseness (%)	Immobility firing rate (Hz)	Animal	Animal state	Reference
Pyramidal	2.31 ± 2.19	2.32 ± 2.10	0.2	Rat	Awake; freely moving	[45]
	19.80 ± 0.21	20.06 ± 0.15	0.5	Rat	Awake; freely moving	[70]
			0.72 ± 0.51	Rat	Urethane-anesthetized	[60]
			CA3a: 0.4 CA3b: 0.3	Rat	Awake; freely moving	[71]
			1.74 ± 1.45	Mice	Awake; freely moving	[72]
Axo-axonic	8.03 ± 0.99	8.40 ± 1.01	22.8 ± 3.1	Rat	Urethane-anesthetized	[57]
	71.67 ± 1.20	73.65 ± 1.29				
Basket	13.53 ± 1.57	14.62 ± 1.23	20 ± 7	Rat	Urethane-anesthetized	[56]
	91.83 ± 2.81	95.31 ± 1.33	17 ± 7*	Rat	Isoflurane-anesthetized	[73]
			8.2 ± 5.6*	Rat	Awake; head-fixed	[74]
Basket CCK+	4.62 ± 0.46	4.75 ± 0.46	0.99	Rat	Urethane-anesthetized	[60]
	42.48 ± 0.68	43.29 ± 0.59				
Bistratified	6.90 ± 0.56	7.18 ± 0.57	0.9 ± 0.26*	Rat	Urethane-anesthetized	[75]
	62.75 ± 1.28	64.59 ± 1.06	30.4*	Rat	Awake; freely moving	[76]
Ivy	2.36 ± 1.22	3.01 ± 1.29	1.7 ± 0.3*	Rat	Urethane-anesthetized	[58]
	22.96 ± 3.82	28.77 ± 3.59	3.0 ± 3.6*	Rat	Awake; freely-moving	
MFA ORDEN	2.79 ± 0.92	3.07 ± 0.94	N/A	---	---	---
	27.05 ± 1.59	29.50 ± 1.71				
QuadD-LM	7.24 ± 0.87	7.58 ± 0.86	6.14	Rat	Urethane-anesthetized	[60]
	66.31 ± 1.32	68.42 ± 1.11				

*These values are from recordings in CA1

(ISI) of individual neurons was correlated with their firing irregularity as measured by the coefficient of variation (CV) of their ISIs [49]. Interestingly, perisomatic neuron types displayed strikingly distinct behaviors in this regard, with Basket, Axo-axonic, and Basket CCK+ cells demonstrating strong positive, no, and weakly negative correlations, respectively, under the synchronous activation of 1,000 Pyramidal cells ($r = 0.83, -0.04$, and -0.38, respectively; Fig. 4c). In contrast, all dendritic-targeting neuron types showed no to weak correlation ($r = -0.05, 0.04, 0.23, -0.18$ for Bistratified, Ivy, MFA ORDEN, and QuadD-LM, respectively; Fig. 4d). For Pyramidal cells, the correlation was moderately positive ($r = 0.40$; Fig. 4e). Moreover, while the correlation coefficients between mean ISI and ISI CV were largely independent of stimulation paradigm for Pyramidal cells, they varied more substantially for interneurons, in particular the perisomatic types (Fig. 4f). Nevertheless, the overall positive values of these coefficients confirmed that neurons with higher mean firing frequencies had lower CV for their ISIs, consistent with previous findings on cortical neurons [49].

The contributions of each neuron type to the LFP were evaluated with spike-to-phase coupling (SPC) relationships. PSD analysis revealed a 16 Hz oscillation in the LFP, which was band-pass filtered within the beta range (10–30 Hz). SPC relationships of each neuron type were then computed relative to the filtered LFP. Pyramidal cells fired before and near the peak of the oscillation, while all interneuron types fired following the Pyramidal cells (Fig. 5a, b). The level of beta modulation exhibited by each neuron type, as quantified through the mean resultant vector length (MRVL), was strongly phase-locked to the beta rhythm ($p < 0.001$, Rayleigh's nonuniformity test) (Fig. 5c). Pyramidal cells fired on average every 7th oscillation, while Basket cells fired nearly every oscillation (Fig. 5d). The correlation of mean firing frequency with phase indicated that neuron types that were more active fired earlier during the dominant oscillation ($r = -0.89$; $p < 0.001$). These results were consistent across the whole range of transient stimulation intensities, from 1% of Pyramidal cells synchronously to 34% asynchronously. Taken together with the firing frequency features of the network's average frequency and corresponding CV, the PSD and SPC feature preservation indicated that the CA3 network was both stable and robust.

To better understand the mechanisms underlying the stability and robustness observed in the baseline network, we modeled two alternative architectures: a *class* network preserving the neuron types but homogenizing the synaptic connectivity and an *archetype* network that simplified

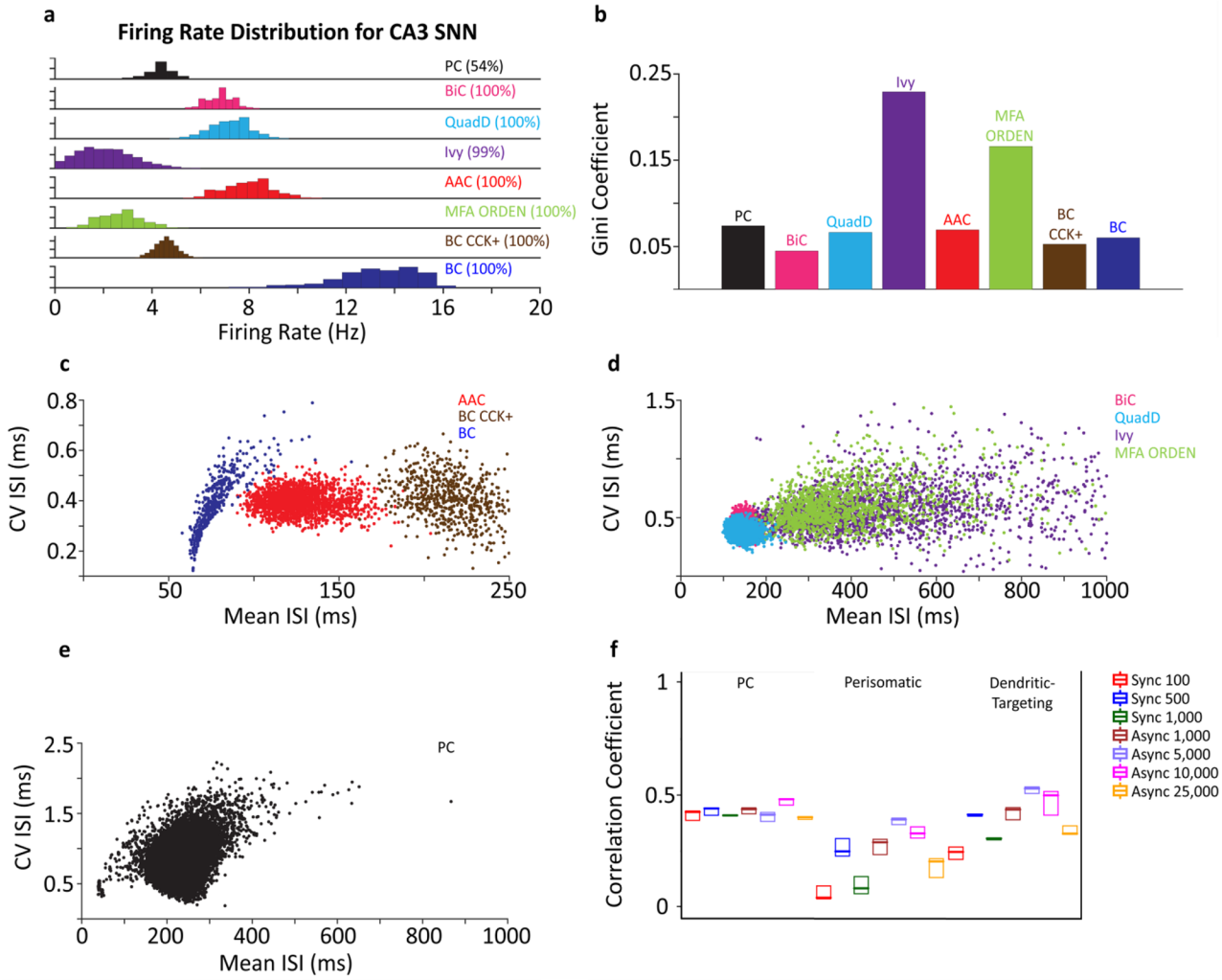

Fig. 4 CA3 spiking neural network firing characteristics. **a** Mean firing rate distributions of the neurons active during the recording window in each type. Percentages in parentheses indicate active fraction. **b** The Gini coefficient shows how unevenly individual neurons contribute to the overall firing rate of their respective type. **c**–**e** Scatter plots of the coefficient of variation (CV) of the ISI of every neuron in each type as a function of its mean ISI displayed for perisomatic (**c**), dendritic-targeting (**d**), and Pyramidal cell types (**e**). **f** Box plot of correlation coefficients for perisomatic, dendritic-targeting, and Pyramidal cell types with varying levels of synchronous and asynchronous network activation

the neuron type composition but preserved their synaptic connectivity. After either synchronous or asynchronous activation, the class network LFP displayed a gradual decrease in voltage, due to the hyperpolarized state of the network's Pyramidal cells (Fig. 6a). Given that Pyramidal cells were the only drivers of excitation in the network, the network firing ceased for the remainder of the simulation. In contrast, the archetype network exhibited elevated mean firing frequencies relative to the baseline network, with a GAF of 6.46 Hz for synchronous activation (Fig. 6c). As for the neuron type representatives, under synchronous activation, the mean firing frequencies of Pyramidal and MFA ORDEN cells increased to 4.93 and 17.78 Hz, respectively, while Basket cells were nearly silenced with a frequency of 0.12 Hz. When subjected to asynchronous activation, Basket cells were silenced entirely (Fig. 6b). Additionally, the CV of the network's firing frequency increased nearly two-fold to 1.34 under synchronous activation (Fig. 6d). The increased firing frequencies within this network variant raised the oscillation frequency only marginally from 16 to 18 Hz for both synchronous and asynchronous activation. SPC relationships to the filtered LFP highlighted surprising differences relative to the baseline. Pyramidal cells fired later during the oscillation, with a phase shift of 25° in the synchronous case, placing the preferred firing phase after the oscillation peak (Table 6). MFA ORDEN, the dendritic-targeting representative type, fired earlier than the perisomatic type representative, the

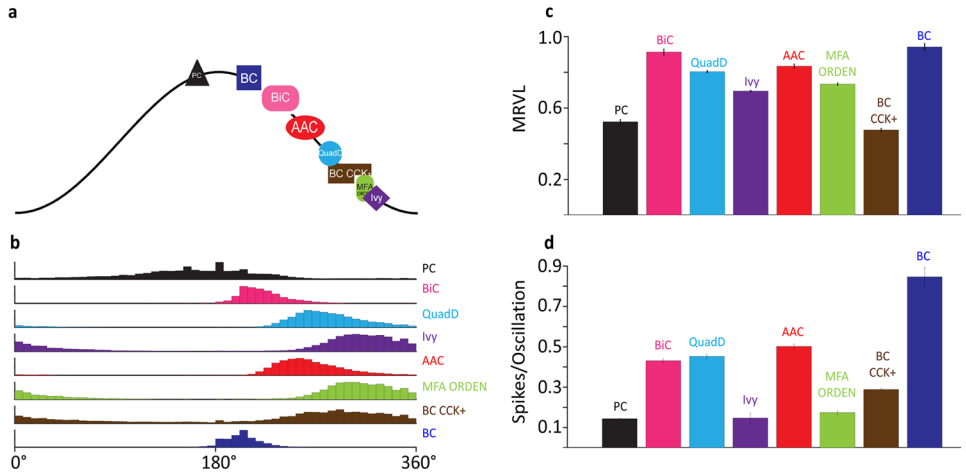

Fig. 5 Intrinsic beta rhythms of the baseline CA3 SNN. **a** Preferred firing phases of each neuron type. **b** Firing phase histograms for each neuron type relative to the network's beta rhythm. **c** Mean resultant vector length (MRVL) for each neuron type exhibit strong phase-locking to the beta rhythm. **d** Mean spikes per oscillation for each neuron type

Basket cells, which in the baseline had the earliest firing phase of any interneuron type. Taken together, the results from the archetype and class networks indicated that the contribution of both individual neuron type properties and connection-type specificity were necessary for network stability and robustness.

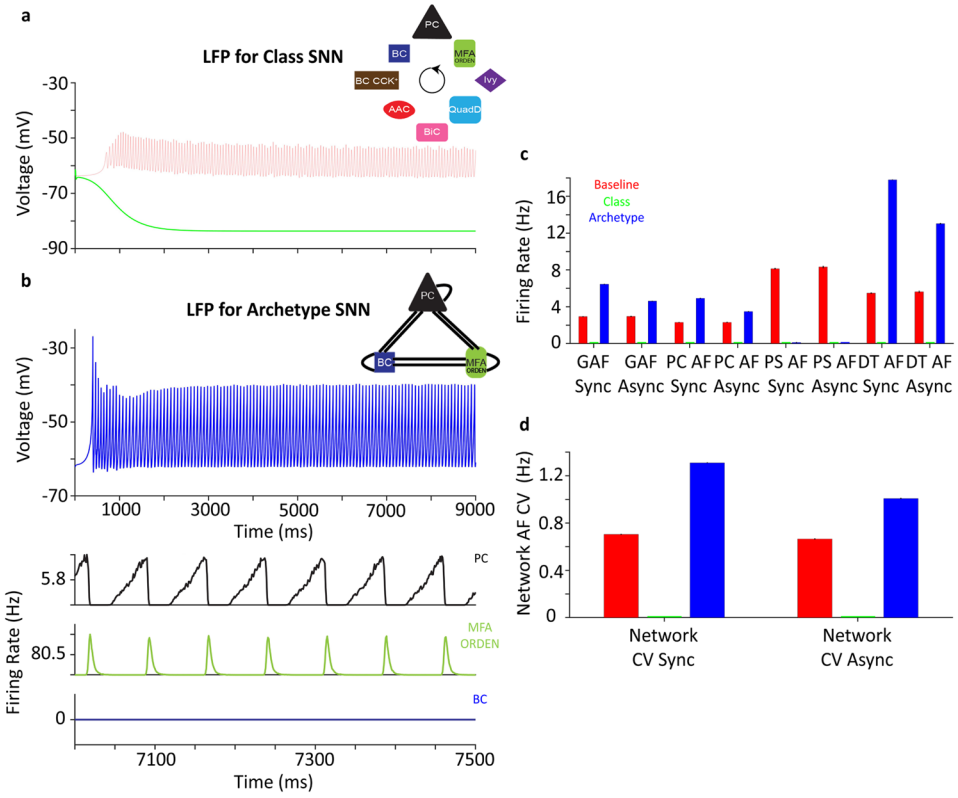

Fig. 6 Alternate networks highlight the importance of both neuron and connection-type specificity. **a** The *class* network LFP is strongly hyperpolarized (green), leading to network silence. Baseline network LFP (faded red) shown for comparison. Inset: Connectivity schematic for the *class* network, with a circular arrow indicative of shuffled connectivity among each connection class. **b** Top: The archetype network LFP (blue) exhibits a beta band oscillation, similar to the baseline. Inset: Connectivity schematic for the archetype network. Bottom: Population firing rates for the Pyramidal cells (top) and MFA ORDEN (middle) show elevated firing rates relative to baseline, but the Basket cells (bottom) are silent. **c** Average firing rate frequencies (AF) of the whole network, Pyramidal, perisomatic-, and dendritic-targeting interneuron types for the baseline (red), class (green), and archetype (blue) network configurations. AFs are robust under synchronous and asynchronous activation for the baseline network, while AFs are not robust for the class and archetype networks. **d** The network AF CV highlights the stability and instability of the baseline and archetype networks, respectively. GAF, grand average frequency; PC, Pyramidal cell; PS, perisomatic; DT, dendritic-targeting; CV, coefficient of variation

Table 6 Preferred firing phases by neuron type for the baseline and archetype networks for synchronous (1,000) and asynchronous (10,000) random Pyramidal cell activation

Neuron type	Synchronous				Asynchronous			
	Baseline		Archetype		Baseline		Archetype	
	Phase (°)	MRVL	Phase (°)	MRVL	Phase (°)	MRVL	Phase (°)	MRVL
CA3 Pyramidal	162	0.51	188	0.69	170	0.55	185	0.68
CA3 Axo-axonic	264	0.83			272	0.85		
CA3 Basket	202	0.93	266	0.96	203	0.95		
CA3 Basket CCK+	304	0.48			314	0.49		
CA3 Bistratified	221	0.90			228	0.92		
CA3 Ivy	322	0.70			326	0.70		
CA3 MFA ORDEN	319	0.73	262	0.98	328	0.73	261	0.97
CA3 QuadD-LM	282	0.80			289	0.81		

The baseline CA3 SNN can be also adapted to test different hypotheses relevant to CA3. To demonstrate the flexibility of our framework in this regard, we updated the baseline SNN by including an additional neuron type, the granule cells of the dentate gyrus (DG Granule), and its corresponding mossy fiber projections to CA3 (Fig. 7a); this updated *DG-CA3* SNN provided an additional 395,000 neurons and 65,000,000 synapses. Instead of synchronous or asynchronous transient input to random Pyramidal cells at the beginning of the simulation, we provided constant input from a population of DG Granule cells. As the baseline network was more representative of an isolated CA3 preparation, we hypothesized that the additional afferent input could elevate the originally observed beta rhythm to an oscillation in the gamma band. Indeed, the resultant network activity of the DG-CA3 network showed a dominant oscillation in the slow gamma range (25–55 Hz, [50]), which persisted across simulations generated from different random seeds (25.3 ± 0.3 Hz; $n = 15$; Fig. 7c). Interestingly, in this model, the Basket cells fired in spike doublets, a phenomenon observed in identified CA3 Basket cells in vitro ([51], Fig. 7d). Similar to those recorded in vitro, the Basket cells in the DG-CA3 SNN had short ISIs during the doublets (8.5 ms in vitro; 4.6 ms in silico) and exhibited a high doublet event rate (6 vs 8 spike doublets in the designated 300 ms time interval). SPC relationships to the filtered LFP largely preserved the phase preferences observed in the beta oscillations for the baseline network (Table 7). These results provide evidence that afferents

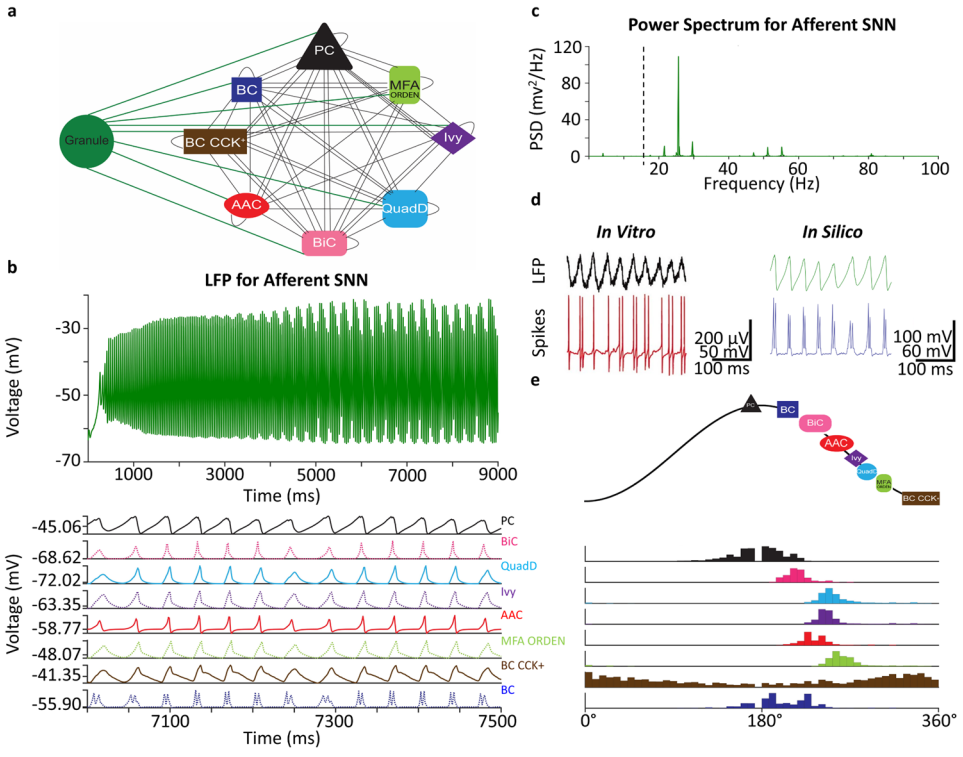

Fig. 7 Addition of Granule cell afferents generates gamma oscillations. **a** Connectivity schematic for the network including granule cell afferents. **b** Top: The DG-CA3 network LFP (green) exhibits oscillations in the slow gamma frequency band. Bottom: LFPs for each neuron type. **c** The power spectrum of the DG-CA3 SNN contains a pronounced peak at 26 Hz, indicative of the network's slow gamma frequency as mediated by the mossy fiber input. Dashed line indicates the spectral peak in the baseline network. **d** Basket cells fire in spike doublets during gamma oscillations in vitro (left), a behavior also exhibited by Basket cells in our simulations (right). **e** Top: Preferred firing phases of each neuron type. Bottom: Firing phase histograms for each neuron type relative to the network's gamma rhythm

Table 7 Preferred firing phases by neuron type for the DG-CA3 network

Neuron type	Phase (°)	MRVL
CA3 Pyramidal	174	0.86
CA3 Axo-axonic	234	0.94
CA3 Basket	200	0.87
CA3 Basket CCK+	345	0.33
CA3 Bistratified	215	0.95
CA3 Ivy	251	0.89
CA3 MFA ORDEN	267	0.88
CA3 QuadD-LM	257	0.89

allow for gamma oscillation generation and highlight that our network can be readily adapted to test different hypotheses regarding area CA3.

Discussion

We leveraged Hippocampome.org to create a data-driven SNN of the mouse hippocampal subregion CA3. To define, instantiate, run, and analyze the simulations, we updated CARLsim4 to allow for synapse-type specific STP and to record the voltage and current of each neuron. Coupled with the ability to record the spike times of individual neurons in a multi-GPU simulation environment, this framework provides a tractable and efficient testing ground to evaluate large-scale, biologically realistic SNN models.

Our network, when provided with transient synchronous or asynchronous stimulation to random subsets of Pyramidal cells, was able to reach and maintain stable and robust rhythmic network activity. Altering the network configuration to reduce or abolish the neuron-type and connection-type specific parameters severely impaired the stability and robustness of the resting-state dynamics. These results highlighted the necessity of neuron and connection-type specificity in the creation of large-scale, data-driven, and biologically realistic networks, as borne out previously in invertebrate model systems [52].

Beyond building a stable and robust data-driven SNN, we aimed to re-create the characteristics for the CA3 network observed in vivo. These characteristics included the mean firing rates for each neuron type, network firing frequency features (i.e., rhythms), and SPC relationships for those network firing frequency features. Considering the mean firing frequencies for defined neuron types, our model reasonably matched the estimates observed when the animal was immobile (Table 5). In particular, Basket, QuadD-LM, and Ivy cells were either within the range or at most ~23% greater than the reported value in vivo. At the same time, Pyramidal and Axo-axonic cells were more than threefold greater and 2.5-fold less than the reported value in vivo, respectively. These mismatches may be due to the network stimulation protocol by single spikes to a randomly activated set of Pyramidal cells, as opposed to continuous afferent excitation.

For CA3, the primary network behaviors exhibited in vivo during immobility are small (SIA) and large irregular activity (LIA), which reflect frequencies in the 0–4 Hz band, and sharp-wave ripples (SWR), which occur at frequencies of 150–200 Hz [5, 50]. We did not observe the former at all in our network and only detected the latter during the population burst of Pyramidal cells (marked as "iii" in Fig. 3a; even here, however, frequencies continuous with beta oscillations displayed greater power than the SWRs). Otherwise, our network generated a 16 Hz beta oscillation, which was surprising given that this frequency band is not commonly reported in hippocampal resting state (see however [53]). We believed this may be due to the absence of sustained extrinsic activity from the entorhinal cortex, dentate gyrus, and other cortical and subcortical areas [54]. To test if the absence of sustained extrinsic activity would be sufficient to reproduce these network behaviors during immobility, we altered the network architecture once more to include mossy fiber afferents from a population of DG Granule cells. The modified DG-CA3 network did not produce SWR, SIA, nor LIA; however, a strong slow gamma oscillation did emerge, which involved synchronized firing between Pyramidal cells and interneurons, leading to sustained excitation of Pyramidal cells that preceded those of interneurons, a feature observed both in vivo and in vitro [55]. In future work, we plan to test our mossy fiber DG-CA3 SNN with additional afferent synapses from the entorhinal cortex to further explore typically observed rhythms such as SWRs or theta.

Our analysis of SPC relationships indicated that Pyramidal cells preferentially fired at the peak of the oscillation, followed by each interneuron type. We noticed that Basket cells fired closest to Pyramidal cells, followed by two other fast-spiking interneuron types, Bistratified, and Axo-axonic cells. More generally, faster spiking cells fired closest to Pyramidal cells, while regular spiking cells fired farthest from the Pyramidal cells (Fig. 5a-b). SPC relationship analysis of the SWRs that CA3 exhibits during rest in vivo indicates that Pyramidal and Basket cells fire near the trough on the descending and ascending phase of the SWR, respectively [56]. Additionally, Axo-axonic and Ivy cells are silent during SWRs, thus having no SPC relationship [57, 58]. Since the oscillations of our model and those observed in vivo are different, we cannot make a direct comparison between their SPC relationships. Furthermore, to our knowledge, there are no SPC relationship analyses for beta rhythms to compare firing phase preferences with in vivo observations.

The SPC relationships during the gamma oscillations observed in our DG-CA3 SNN could also be compared with

a previous in vitro study [59]. Reconstructed Pyramidal cells and interneurons fired on the ascending phase of the oscillation, with Pyramidal cell spikes preceding those of the interneurons. While the phase preferences of the identified Pyramidal, perisomatic-, and dendritic-targeting types were earlier than those in our SNN, the firing phase preference order was preserved (Pyramidal spikes preceding interneuron spikes). The residual quantitative discrepancy is not surprising given the different (carbachol-induced) activation protocol in this experimental preparation relative to our simulation. Additionally, we noticed that Basket CCK+ cells were not strongly phase-locked to gamma oscillations in our network, as observed for these cells in vivo [60]. If Basket CCK+ cells fire asynchronously, then they can release neurotransmitters asynchronously as well. Thus, our results support the hypothesis that asynchronous GABA release from Basket CCK+ terminal boutons could be an emergent property of hippocampal networks [61].

The choice of the Izhikevich formalism for neuron models enabled the implementation of a full-scale network of the CA3 circuit but substantially limits the opportunity to investigate how non-linear dendritic integration in Pyramidal neurons may affect the information-processing capabilities of the networks as a whole. Early multi-compartment models of CA3 Pyramidal cells allowed a detailed investigation of the spatial–temporal interplay of passive and active membrane properties underlying bursting behavior in these neurons [62]. Pairing experimental in vitro recordings with multi-compartmental simulations showed that the diversity of intrinsic dynamics in CA3 Pyramidal neurons (bursting, early-onset adapting, and late-onset non-adapting) may be explained by relative differences in potassium currents [63]. The emergent properties of a simulated network of multi-compartment neuron models could undoubtedly enhance the integrative properties of incoming input, whether noisy or periodic. A seminal CA3 network model of 1200 multi-compartment neurons replicated features of the in vivo network such as theta-modulated gamma and low mean firing rates with neurons not firing every cycle [64]. That simulation reflected considerably less cellular and circuit diversity than ours, with only three neuron types (Pyramidal, Basket, and O-LM). Whether a network simulation composed of a more representative diversity of single-compartment neurons could also reproduce those dynamic features remains to be shown in future modeling work.

The primary reason for adopting a single-compartment approach in this work was the computational feasibility of studying the dynamics of the entire CA3 circuit at scale. CARLsim4 is highly optimized for large-scale spiking neural network simulations on GPUs and has reported up to 60× speedup for multi-GPU implementations [28]. However, CARLsim4 is limited to Izhikevich and leaky integrate-and-fire (LIF) formalisms. Notably, Hippocampome.org does offer multi-compartment Izhikevich formalisms for modeling neuronal input–output relations [19]. While CARLsim4 provides GPU support for simple multi-compartment Izhikevich neurons that model the interaction among compartments, this formalism does not capture full neuronal morphologies or precise compartment geometry. This may be a limitation for users that are interested in how dendritic arbors influence computation. However, even in different simulation environments, memory constraints generally limit the network size of complex multi-compartmental models implemented in GPUs. For example, using CoreNEURON, a GPU-compatible simulation environment, large-scale networks of the rat somatosensory cortex and CA1 with multi-compartment neurons could only be modeled on CPUs and were proven to be unfeasible on GPUs due to memory limitations [65]. As GPU speed and on-board memory increases in future hardware architectures, it may soon become practical to simulate a whole CA3 circuit with multi-compartment neuron models.

The minimally invasive and transient stimulation protocol chosen provided an effective and efficient way to assess CA3 resting-state dynamics, whereas continuous periodic or noisy input from external afferents would have complicated the interpretation of resting-state activity. The robustness observed in our model, as characterized by the convergence of the network to a stable and periodic activity pattern independent of the transient stimuli provided, highlights the auto-associative capability of CA3. Notably, our simulation design approximated away the anatomically realistic topographic organization of this circuit which was included in another recent model [66]. Instead, the network dynamic was critically dependent on the network circuitry which utilized neuron type-specific connection probability estimates. This result highlights that the key information processing element in neural circuits may be neuron types and their potential connections, as opposed to topographic connectivity.

Among the key conceptual elements not yet implemented in this SNN simulation of CA3 is long-term plasticity (LTP): the synaptic weights in our network model were fixed within each pair of neuron types and fully determined by the TPM model. The main reason for this exclusion is again the absence of sufficient experimental constraints in this regard for most pairs of neuron types in the model. Nonetheless, our framework is flexible enough to incorporate LTP through spike-time-dependent plasticity, whose implementation in future network models may be sufficient to reproduce the non-uniform distribution of weights observed in the hippocampus [67]. Similarly, we did not model spatially selective inputs, which in later extensions of this work might foster a better understanding of state transitions between different network rhythms and the contribution of individual neuron types to the formation of CA3 Pyramidal cell place fields. Furthermore, including other conceptual circuit building blocks such as neuromodulation

Table 8 Conceptual elements for building full-scale network models

	Conceptual element	Limitations if modeled or rationale for exclusion	Advantages of the element
Modeled	Neuron types	Eight neuron types were included in our model as representatives of the majority of supertypes in CA3. However, we have not included all 25 defined neuron types in the subregion	Provides strong explanatory power as to how cells classified by morphology, primary neurotransmitter, and molecular markers contribute to the network dynamics
	Population sizes for each neuron type	Each included neuron type adopts the population size of the represented supertype	Provides strong mechanistic constraints regarding the relative proportions of neuron types within the modeled circuit
	Input–output relationships for each neuron type	See "Diversity of input–output relationships" and "Input–output relationships modeled through a multi-compartment formalism" below	Employing Izhikevich models for each neuron type allows for lower computational cost while preserving the realistically diverse firing patterns observed experimentally
	Connection probabilities between neuron types	Hippocampome.org provides probabilities for all local-circuit axonal-dendritic connections. We employed reasonable assumptions to estimate long-range and perisomatic connections	Realistic connection probability estimates strongly constrain activity pattern propagation through the network
	Short-term synaptic dynamics based on fast receptor currents	N/A	Inclusion of short-term synaptic dynamics accounts for synaptic depression and facilitation observed in hippocampal networks, as well as the failure rate of transmitter release
	Conductance delays	Conductance delays were computed based on the somatic distances of axons within the individual CA3 layers and an assumed conductance velocity. These delays were rounded at the precision of 1 ms, whereas intra-layer conductance delays may be shorter	Estimates of conductance delays allow for activity patterns to propagate through the network following similar constraints as imposed in a real mouse hippocampus. Conductance delays may be important to binding of neurons into cell assemblies [77]
Excluded	Long-term plasticity (LTP)	We do not have connection-type specific data to constrain estimates for LTP nor information about connection-type specific learning rules. Thus, we used fixed rather than plastic synaptic weights in our network models	LTP in network models allows for new information to be stored, updated, or removed via synaptic weight changes. An understanding of how LTP works across individual connection types or classes could be crucial to understanding hippocampal memory processes
	Diversity of input–output relationships (i.e., including multiple firing patterns for defined neuron types)	We do have multiple Izhikevich parameter sets for the Pyramidal and Bistratified cells but opted not to include them to simplify the interpretation of network dynamics. We plan to include these parameter sets in future modeling work	Neurons of the same type can vary in their spiking response to the same input pattern. Incorporating this diversity in network models may clarify the mechanism of different network activity states
	Input–output relationships modeled through a multi-compartment formalism	We do have Izhikevich parameter sets optimized for multiple compartments but opted not to include them to limit computational cost. We plan to include these parameter sets in future modeling work	Neurons consist of multiple structural elements: a soma, dendrites, and an axon. Network models that contain multi-compartment based neurons may be important for replicating hippocampal functions observed in vivo, such as theta-nested gamma oscillations during memory storage and retrieval [64, 78]
	Short-term synaptic dynamics based on both fast and slow receptor currents (e.g., NMDA and $GABA_B$)	We do not yet have enough data available to constrain the slow components of short-term synaptic signals	Network models that incorporate both fast (e.g., AMPA and $GABA_A$) and slow (e.g., NMDA and $GABA_B$) current types could better reproduce distinct network oscillations

Table 8 (continued)

Conceptual element	Limitations if modeled or rationale for exclusion	Advantages of the element
Neuromodulatory effects on synaptic dynamics	We do not yet have enough data available to incorporate the effects of neuromodulation at each connection type	Hippocampal neurons express receptors for serotonin, dopamine, acetylcholine, and other neuromodulators [79]. These receptors influence synaptic gain and plasticity [80]. Network models that employ connection-type specific neuromodulation could thus be critical to elucidate those operations
Higher order connectivity motifs	We do not yet have estimates for the frequencies of occurrence of connectivity motifs at the level of individual neurons	Incorporating realistic connectivity motifs between neurons [81] could lead to more robust network models of pattern completion [82]
Embedding of network in more than one spatial dimension	We do not yet have data to constrain the connection probabilities between neuron types in greater than one dimension	Models that can account for the 3D embedding of hippocampal neurons and their connectivity could better capture functional dynamics [83]

or diverse input–output relationships for each neuron type may contribute to elucidate CA3 functionality (Table 8). While experimental estimates are still lacking for many of these conceptual building blocks, explicitly modeling each one with the Hippocampome-CARLsim4 framework may help establish reasonable bounds.

Our network modeling approach serves as a steppingstone towards building both a powerful comparison and prediction framework for hypotheses of CA3 functions. Measurement of the phase preferences of Pyramidal cells and a variety of perisomatic- and dendritic-targeting interneuron types can be made, allowing for comparisons with unique neuron types recorded in various experimental settings and generating experimentally testable predictions for those neuron types that still lack direct evidence [68]. Additionally, this framework can predict and explain emergent network behavior, as in the example of the circuit level mechanism for asynchronous vesicle release. Last but not least, the SNN simulation size and connectivity can be scaled down to reproduce and be more directly compared to the in vitro slice model system for exploring similarities and differences with experimentally tractable circuit interactions [69]. This will then provide a fuller picture of how a variety of interneuron types create the observed dynamics in area CA3.

Conclusion

The large-scale CA3 SNN we have developed here serves as an important milestone in the Hippocampome.org project: the creation of a data-driven neural circuit model of a hippocampal subregion that integrates biologically realistic parameter estimates for the population sizes and intrinsic properties of defined hippocampal neuron types as well as the connection probabilities and STP between them. All parameter estimates and the software to create, simulate, and analyze this model are well-documented and freely available on the CARLsim and Hippocampome.org GitHub (github.com/UCI-CARL/CARLsim4/tree/feat/meansdSTPPost_hc/projects; github.com/Hippocampome-Org/snn_analysis), in line with our commitment to open science. While Hippocampome parameter estimates are manually transferred to CARLsim4 in the current CARLsim4-Hippocampome framework, automation of parameter transfer will be forthcoming in the next major release of Hippocampome. In future work, this flexible framework will allow further investigations of the computations performed by the under-explored subregion CA3. Afferent excitation can be supplied from both the dentate gyrus and the entorhinal cortex to simulate theta and gamma rhythms, SWRs, and measure SPC relationships for each neuron type. The involvement of every neuron type for each rhythm can be further examined by modifying parameter estimates such as population sizes and connection strengths. How CA3 performs the functions

of pattern completion and auto-association can also be tested, either through input patterns of excitation or images converted to input spike trains to random sets of Pyramidal cells. Moreover, data-driven network simulations can be extended to other under-explored areas of the hippocampus, such as CA2 and subiculum, advancing towards the goal of a full scale SNN of the entire hippocampal formation.

Acknowledgements The authors are grateful to Drs. Diek Wheeler, David Hamilton, and Siva Venkadesh for helpful discussions.

Author Contribution JDK and GAA designed and conceptualized the study. CT and KM provided parameter estimates related to connectivity and short-term plasticity of the connection types, respectively. SMA provided the parameter estimates for the population sizes of the neuron types. HJK, JX, and KC updated CARLsim to allow connection-type specificity between neuron types and the recording of the instantaneous membrane potential and input current for all neurons in our network model. JLK oversaw the development of the CARLsim updates. JDK wrote the software to create, simulate, and analyze the network. JDK and GAA analyzed the data and wrote the manuscript with feedback from CT, KM, SMA, and JLK.

Funding This research was supported in part by the National Institutes of Health through grants U01MH114829 (BICCN) and R01NS39600.

Declarations

Ethics Approval This article does not contain any studies with human participants or animals performed by any of the authors.

Informed Consent Informed consent was not required as no humans or animals were involved.

Conflict of Interest The authors declare no competing interests.

References

1. Scoville WB, Milner B. Loss of recent memory after bilateral hippocampal lesions. J Neurol Neurosurg Psychiatry. 1957;20(1):11–21.
2. Nadel L, Moscovitch M. Memory consolidation retrograde amnesia and the hippocampal complex. Curr Opin Neurobiol. 1997;7(2):217–27.
3. Wang S-H, Morris RGM. Hippocampal-neocortical interactions in memory formation consolidation and reconsolidation. Annu Rev Psychol. 2010;61(1):49–79.
4. Vanderwolf CH. Hippocampal electrical activity and voluntary movement in the rat. Electroencephalogr Clin Neurophysiol. 1969;26(4):407–18.
5. Buzsáki G. Hippocampal sharp wave-ripple: a cognitive biomarker for episodic memory and planning. Hippocampus. 2015;25(10):1073–188.
6. Murakami TC, Mano T, Saikawa S, Horiguchi SA, Shigeta D, Baba K, et al. A three-dimensional single-cell-resolution whole-brain atlas using CUBIC-X expansion microscopy and tissue clearing. Nat Neurosci. 2018;21(4):625–37.
7. Zhu F, Cizeron M, Qiu Z, Benavides-Piccione R, Kopanitsa MV, Skene NG, et al. Architecture of the mouse brain synaptome. Neuron. 2018;99(4):781–99.
8. Armañanzas R, Ascoli GA. Towards the automatic classification of neurons. Trends Neurosci. 2015;38(5):307–18.
9. The Petilla Interneuron Nomenclature Group (PING), Ascoli GA, Alonso-Nanclares L, Anderson SA, Barrionuevo G, Benavides-Piccione R, et al. Petilla terminology: nomenclature of features of GABAergic interneurons of the cerebral cortex. Nat Rev Neurosci. 2008;9(7):557–68.
10. Wheeler DW, White CM, Rees CL, Komendantov AO, Hamilton DJ, Ascoli GA. Hippocampome.org: a knowledge base of neuron types in the rodent hippocampus. elife. 2015;4:e09960.
11. Ascoli GA, Wheeler DW. In search of a periodic table of the neurons: axonal-dendritic circuitry as the organizing principle. BioEssays. 2016;38(10):969–76.
12. Rees CL, Moradi K, Ascoli GA. Weighing the evidence in Peters' rule: does neuronal morphology predict connectivity? Trends Neurosci. 2017;40(2):63–71.
13. Moradi K, Ascoli GA. Systematic data mining of hippocampal synaptic properties. In: Cutsuridis V, Graham BP, Cobb S, Vida I, editors. Hippocampal Microcircuits: A Computational Modeler's Resource Book. Cham: Springer International Publishing; 2018. p. 441–71 (Springer Series in Computational Neuroscience).
14. Rees CL, Wheeler DW, Hamilton DJ, White CM, Komendantov AO, Ascoli GA. Graph theoretic and motif analyses of the hippocampal neuron type potential connectome. eNeuro. 2016;3(6).
15. White CM, Rees CL, Wheeler DW, Hamilton DJ, Ascoli GA. Molecular expression profiles of morphologically defined hippocampal neuron types: empirical evidence and relational inferences. Hippocampus. 2020;30(5):472–87.
16. Komendantov AO, Venkadesh S, Rees CL, Wheeler DW, Hamilton DJ, Ascoli GA. Quantitative firing pattern phenotyping of hippocampal neuron types. Sci Rep. 2019;9:17915.
17. Ascoli GA. The coming of age of the hippocampome. Neuroinformatics. 2010;8(1):1–3.
18. Attili SM, Silva MFM, Nguyen T, Ascoli GA. Cell numbers distribution shape and regional variation throughout the murine hippocampal formation from the adult brain Allen Reference Atlas. Brain Struct Funct. 2019;224(8):2883–97.
19. Venkadesh S, Komendantov AO, Listopad S, Scott EO, De Jong K, Krichmar JL, et al. Evolving simple models of diverse intrinsic dynamics in hippocampal neuron types. Front Neuroinform. 2018;12:8.
20. Tecuatl C, Wheeler DW, Sutton N, Ascoli GA. Comprehensive estimates of potential synaptic connections in local circuits of the rodent hippocampal formation by axonal-dendritic overlap. J Neurosci. 2021;41(8):1665–83.
21. Moradi K, Ascoli GA. A comprehensive knowledge base of synaptic electrophysiology in the rodent hippocampal formation. Hippocampus. 2020;30(4):314–31.
22. Dehghani N, Peyrache A, Telenczuk B, Le Van QM, Halgren E, Cash SS, et al. Dynamic balance of excitation and inhibition in human and monkey neocortex. Sci Rep. 2016;6(1):23176.
23. He H, Cline HT. What is excitation/inhibition and how is it regulated? A case of the elephant and the wisemen. J Exp Neurosci. 2019;13.
24. Dyhrfjeld-Johnsen J, Santhakumar V, Morgan RJ, Huerta R, Tsimring L, Soltesz I. Topological determinants of epileptogenesis in large-scale structural and functional models of the dentate gyrus derived from experimental data. J Neurophysiol. 2007;97(2):1566–87.
25. Hendrickson PJ, Yu GJ, Song D, Berger TW. A million-plus neuron model of the hippocampal dentate gyrus: dependency of spatio-temporal network dynamics on topography. Conf Proc IEEE Eng Med Biol Soc. 2015;2015:4713–6.
26. Bezaire MJ, Soltesz I. Quantitative assessment of CA1 local circuits: knowledge base for interneuron-pyramidal cell connectivity. Hippocampus. 2013;23(9):751–85.

27. Yu GJ, Feng Z, Berger TW. Network activity due to topographic organization of Schaffer collaterals in a large-scale model of rat CA1. Conf Proc IEEE Eng Med Biol Soc. 2019;2019:2977–80.
28. Chou T, Kashyap HJ, Xing J, Listopad S, Rounds EL, Beyeler M, et al. CARLsim 4: an open source library for large scale biologically detailed spiking neural network simulation using heterogeneous clusters. In: 2018 International Joint Conference on Neural Networks (IJCNN). 2018. p. 1–8.
29. Izhikevich EM. Dynamical Systems in Neuroscience. Cambridge: MIT Press; 2007. p. 522.
30. Venkadesh S, Komendantov AO, Wheeler DW, Hamilton DJ, Ascoli GA. Simple models of quantitative firing phenotypes in hippocampal neurons: comprehensive coverage of intrinsic diversity. PLOS Comput Biol. 2019;15(10):e1007462.
31. Attili SM, Mackesey ST, Ascoli GA. Operations research methods for estimating the population size of neuron types. Ann Oper Res. 2020;289(1):33–50.
32. Attili SM, Wheeler DW, Moradi K, Ascoli GA. Quantification of neuron types in the rodent hippocampal formation by data mining and numerical optimization. bioRxiv. 2021. https://doi.org/10.1101/2021.09.20.460986.
33. Mongillo G, Barak O, Tsodyks M. Synaptic theory of working memory. Science. 2008;319(5869):1543–6.
34. Senn W, Markram H, Tsodyks M. An algorithm for modifying neurotransmitter release probability based on pre- and postsynaptic spike timing. Neural Comput. 2001;13(1):35–67.
35. Tsodyks M, Pawelzik K, Markram H. Neural networks with dynamic synapses. Neural Comput. 1998;10(4):821–35.
36. Tecuatl C, Wheeler DW, Ascoli GA. A method for estimating the potential synaptic connections between axons and dendrites from 2D neuronal images. Bio-Protoc. 2021;11(13):e4073–e4073.
37. Soleng AF, Raastad M, Andersen P. Conduction latency along CA3 hippocampal axons from rat. Hippocampus. 2003;13(8):953–61.
38. Sosa M, Joo HR, Frank LM. Dorsal and ventral hippocampal sharp-wave ripples activate distinct nucleus accumbens networks. Neuron. 2020;105(4):725–41.
39. Taxidis J, Coombes S, Mason R, Owen MR. Modeling sharp wave-ripple complexes through a CA3-CA1 network model with chemical synapses. Hippocampus. 2012;22(5):995–1017.
40. Willmore B, Tolhurst DJ. Characterizing the sparseness of neural codes. Network. 2001;12(3):255–70.
41. Berens P. CircStat: A MATLAB toolbox for circular statistics. J Stat Softw. 2009;31(1):1–21.
42. Bezaire MJ, Raikov I, Burk K, Vyas D, Soltesz I. Interneuronal mechanisms of hippocampal theta oscillations in a full-scale model of the rodent CA1 circuit. eLife. 2016;5:e18566.
43. Gerstner W, Kistler WM, Naud R, Paninski L. Neuronal dynamics: from single neurons to networks and models of cognition. Cambridge: Cambridge University Press; 2014. p. 591.
44. Evstratova A, Tóth K. Information processing and synaptic plasticity at hippocampal mossy fiber terminals. Front Cell Neurosci. 2014;8:28.
45. Mizuseki K, Buzsáki G. Preconfigured skewed distribution of firing rates in the hippocampus and entorhinal cortex. Cell Rep. 2013;4(5):1010–21.
46. Marr D. Vision: a computational investigation into the human representation and processing of visual information. Cambridge: MIT Press; 1982. p. 428.
47. Kriegeskorte N, Douglas PK. Cognitive computational neuroscience. Nat Neurosci. 2018;21(9):1148–60.
48. Jinno S, Kosaka T. Stereological estimation of numerical densities of glutamatergic principal neurons in the mouse hippocampus. Hippocampus. 2010;20(7):829–40.
49. Shadlen MN, Newsome WT. The variable discharge of cortical neurons: implications for connectivity computation and information coding. J Neurosci. 1998;18(10):3870–96.
50. Colgin LL. Rhythms of the hippocampal network. Nat Rev Neurosci. 2016;17(4):239–49.
51. Dugladze T, Schmitz D, Whittington MA, Vida I, Gloveli T. Segregation of axonal and somatic activity during fast network oscillations. Science. 2012;336(6087):1458–61.
52. Huang Y-C, Wang C-T, Su T-S, Kao K-W, Lin Y-J, Chuang C-C, et al. A Single-Cell Level and Connectome-Derived Computational Model of the Drosophila Brain. Front Neuroinform. 2019;12:99.
53. Trimper JB, Galloway CR, Jones AC, Mandi K, Manns JR. Gamma oscillations in rat hippocampal subregions dentate gyrus, CA3, CA1, and subiculum underlie associative memory encoding. Cell Rep. 2017;21(9):2419–32.
54. Sullivan D, Csicsvari J, Mizuseki K, Montgomery S, Diba K, Buzsáki G. Relationships between hippocampal sharp waves, ripples, and fast gamma oscillation: influence of dentate and entorhinal cortical activity. J Neurosci. 2011;31(23):8605–16.
55. ter Wal M, Tiesinga P. Hippocampal oscillations mechanisms (PING ING Sparse). In: Jaeger D, Jung R, editors. Encyclopedia of Computational Neuroscience. New York: Springer; 2013. p. 1–14.
56. Tukker JJ, Lasztóczi B, Katona L, Roberts JDB, Pissadaki EK, Dalezios Y, et al. Distinct dendritic arborization and in vivo firing patterns of parvalbumin-expressing basket cells in the hippocampal area CA3. J Neurosci. 2013;33(16):6809–25.
57. Viney TJ, Lasztoczi B, Katona L, Crump MG, Tukker JJ, Klausberger T, et al. Network state-dependent inhibition of identified hippocampal CA3 axo-axonic cells in vivo. Nat Neurosci. 2013;16(12):1802–11.
58. Fuentealba P, Begum R, Capogna M, Jinno S, Márton LF, Csicsvari J, et al. Ivy cells: a population of nitric-oxide-producing, slow-spiking GABAergic neurons and their involvement in hippocampal network activity. Neuron. 2008;57(6):917–29.
59. Hájos N, Pálhalmi J, Mann EO, Németh B, Paulsen O, Freund TF. Spike timing of distinct types of GABAergic Interneuron during hippocampal gamma oscillations in vitro. J Neurosci. 2004;24(41):9127–37.
60. Lasztóczi B, Tukker JJ, Somogyi P, Klausberger T. Terminal field and firing selectivity of cholecystokinin-expressing interneurons in the hippocampal CA3 area. J Neurosci. 2011;31(49):18073–93.
61. Hefft S, Jonas P. Asynchronous GABA release generates long-lasting inhibition at a hippocampal interneuron–principal neuron synapse. Nat Neurosci. 2005;8(10):1319–28.
62. Lazarewicz MT, Migliore M, Ascoli GA. A new bursting model of CA3 pyramidal cell physiology suggests multiple locations for spike initiation. Biosystems. 2002;67(1):129–37.
63. Hemond P, Epstein D, Boley A, Migliore M, Ascoli GA, Jaffe DB. Distinct classes of pyramidal cells exhibit mutually exclusive firing patterns in hippocampal area CA3b. Hippocampus. 2008;18(4):411–24.
64. Neymotin SA, Lazarewicz MT, Sherif M, Contreras D, Finkel LH, Lytton WW. Ketamine disrupts theta modulation of gamma in a computer model of hippocampus. J Neurosci. 2011;31(32):11733–43.
65. Kumbhar P, Hines M, Fouriaux J, Ovcharenko A, King J, Delalondre F, et al. CoreNEURON: an optimized compute engine for the NEURON simulator. Front Neuroinform. 2019;13:63.
66. Yu GJ, Bouteiller J-MC, Berger TW. Topographic organization of correlation along the longitudinal and transverse axes in rat hippocampal CA3 due to excitatory afferents. Front Comput Neurosci. 2020;14:588881.
67. Zheng P, Dimitrakakis C, Triesch J. Network self-organization explains the statistics and dynamics of synaptic connection strengths in cortex. PLOS Comput Biol. 2013;9(1):e1002848.
68. Sanchez-Aguilera A, Wheeler DW, Jurado-Parras T, Valero M, Nokia MS, Cid E, et al. An update to Hippocampome.org by integrating single-cell phenotypes with circuit function in vivo. PLOS Biol. 2021;19(5):e3001213.

69. Oren I, Mann EO, Paulsen O, Hájos N. Synaptic currents in anatomically identified CA3 neurons during hippocampal gamma oscillations in vitro. J Neurosci. 2006;26(39):9923–34.
70. Kay K, Sosa M, Chung JE, Karlsson MP, Larkin MC, Frank LM. A hippocampal network for spatial coding during immobility and sleep. Nature. 2016;531(7593):185–90.
71. Oliva A, Fernández-Ruiz A, Buzsáki G, Berényi A. Spatial coding and physiological properties of hippocampal neurons in the Cornu Ammonis subregions. Hippocampus. 2016;26(12):1593–607.
72. Ding L, Chen H, Diamantaki M, Coletta S, Preston-Ferrer P, Burgalossi A. Structural correlates of CA2 and CA3 pyramidal cell activity in freely-moving mice. J Neurosci. 2020;40(30):5797–806.
73. Lapray D, Lasztoczi B, Lagler M, Viney TJ, Katona L, Valenti O, et al. Behavior-dependent specialization of identified hippocampal interneurons. Nat Neurosci. 2012;15(9):1265–71.
74. Varga C, Golshani P, Soltesz I. Frequency-invariant temporal ordering of interneuronal discharges during hippocampal oscillations in awake mice. PNAS. 2012;109(40):E2726–34.
75. Klausberger T, Márton LF, Baude A, Roberts JDB, Magill PJ, Somogyi P. Spike timing of dendrite-targeting bistratified cells during hippocampal network oscillations in vivo. Nat Neurosci. 2004;7(1):41–7.
76. Katona L, Lapray D, Viney TJ, Oulhaj A, Borhegyi Z, Micklem BR, et al. Sleep and movement differentiates actions of two types of somatostatin-expressing GABAergic interneuron in rat hippocampus. Neuron. 2014;82(4):872–86.
77. Izhikevich EM. Polychronization: computation with spikes. Neural Comput. 2006;18(2):245–82.
78. Lisman JE, Jensen O. The Theta-gamma neural code. Neuron. 2013;77(6):1002–16.
79. Josh Lawrence J, Cobb S. Neuromodulation of hippocampal cells and circuits. In: Cutsuridis V, Graham BP, Cobb S, Vida I, editors. Hippocampal Microcircuits: A Computational Modeler's Resource Book. New York: Springer International Publishing; 2018. p. 227–325 (Springer Series in Computational Neuroscience).
80. Nadim F, Bucher D. Neuromodulation of neurons and synapses. Curr Opin Neurobiol. 2014;29:48–56.
81. Sporns O, Kötter R. Motifs in Brain Networks. PLOS Biol. 2004;2(11):e369.
82. Guzman SJ, Schlögl A, Frotscher M, Jonas P. Synaptic mechanisms of pattern completion in the hippocampal CA3 network. Science. 2016;353(6304):1117–23.
83. Patel J, Fujisawa S, Berényi A, Royer S, Buzsáki G. Traveling theta waves along the entire septotemporal axis of the hippocampus. Neuron. 2012;75(3):410–7.